Correspondence

Improving Thermal Ablation Delineation With Electrode Vibration Elastography Using a Bidirectional Wave Propagation Assumption

Ryan J. DeWall, *Student Member, IEEE*,
and Tomy Varghese, *Senior Member, IEEE*

***Abstract*—Thermal ablation procedures are commonly used to treat hepatic cancers and accurate ablation representation on shear wave velocity images is crucial to ensure complete treatment of the malignant target. Electrode vibration elastography is a shear wave imaging technique recently developed to monitor thermal ablation extent during treatment procedures. Previous work has shown good lateral boundary delineation of ablated volumes, but axial delineation was more ambiguous, which may have resulted from the assumption of lateral shear wave propagation. In this work, we assume both lateral and axial wave propagation and compare wave velocity images to those assuming only lateral shear wave propagation in finite element simulations, tissue-mimicking phantoms, and bovine liver tissue. Our results show that assuming bidirectional wave propagation minimizes artifacts above and below ablated volumes, yielding a more accurate representation of the ablated region on shear wave velocity images. Area overestimation was reduced from 13.4% to 3.6% in a stiff-inclusion tissue-mimicking phantom and from 9.1% to 0.8% in a radio-frequency ablation in bovine liver tissue. More accurate ablation representation during ablation procedures increases the likelihood of complete treatment of the malignant target, decreasing tumor recurrence.**

I. Introduction

An increase in tissue stiffness often correlates with an underlying tissue pathology [1], and physicians use this to their benefit to detect abnormal tissue via manual palpation. However, the sensitivity and subjectivity of human touch may prevent stiffness changes from being utilized effectively in many cases. Some diseases, such as liver fibrosis [2], cause stiffness to change gradually over time, and some pathologies, such as small hepatic tumors, might not be detectable because of overlying normal tissue.

Several shear wave imaging techniques have been developed that exploit the proportionality of shear wave velocity to the shear modulus, a measure of the inherent stiffness of a material. This is done to quantify the stiffness feature more objectively, providing repeatable and more sensitive stiffness estimates than can be obtained by manual palpation alone. Shear wave generation is typically accomplished by either external mechanical excitation or acoustic radiation force, and the resulting wave is tracked using ultrasound or magnetic resonance imaging [3]–[10].

Manuscript received August 2, 2011; accepted November 9, 2011. This work was supported in part by the National Institutes of Health under grants R01 CA112192-04, R01 CA112192-S103, and T32 CA09206-31.

The authors are with the Departments of Medical Physics and Biomedical Engineering, University of Wisconsin–Madison, Madison, WI (e-mail: dewall@wisc.edu).

Digital Object Identifier 10.1109/TUFFC.2012.2169

Internal mechanical vibration is a shear wave generation method that is advantageous because the shear wave source is deep within the material being imaged. Shear wave amplitude decays rapidly, and shear waves generated by either external vibration or radiation force methods may fail to penetrate into deeper tissue. Internal mechanical vibration has been accomplished in phantoms and hydrogels using a needle as the vibration device [11], [12]. We have developed a technique to be used during thermal ablation procedures called electrode vibration elastography, which uses the vibration of the thermal ablation needle as the shear wave source [13], ultrasound-based tracking, and shear wave velocity reconstruction using the time-to-peak algorithm [7].

Electrode vibration elastography has shown good lateral boundary delineation but more ambiguity above and below the ablation because of high shear wave velocity artifacts, which likely result from the assumption of lateral shear wave propagation. Shear waves generated by electrode vibration elastography primarily propagate laterally; however, time-to-peak images suggest that a wave is also propagating axially, which may explain the artifacts present when using a purely lateral propagation assumption. In this study, we investigate wave propagation in two directions using finite element analysis, tissue-mimicking (TM) phantoms, and bovine liver tissue to minimize artifacts and improve ablation boundary delineation. We calculate both lateral and axial gradients of the time-to-peak image, compare both gradients, make a binary decision of wave propagation direction, and generate a wave velocity image from the combined gradient image. The wave velocity images assuming bidirectional or purely lateral propagation are then compared.

II. Materials and Methods

A. Finite Element Analysis, Phantom, and Ex Vivo Experiments

A finite element model was used to investigate shear wave propagation direction; it simulated the solid-inclusion TM phantom used for electrode vibration elastography, described previously [13]. The phantom consisted of a 30 × 19 mm stiff inclusion in a 120 × 120 mm softer background. The model material properties were based on mechanical testing estimates from a TM phantom material. The electrode was modeled as gold, and the TM materials were 28 kPa (shear wave speed 3.06 m/s) in the inclusion and 7.75 kPa (shear wave speed 1.61 m/s) in the background. An axisymmetric finite element model was created in ANSYS (ANSYS Inc., Canonsburg, PA) using PLANE 183 elements. The bottom of the model was fixed in the x- (lateral) and y- (axial) directions, whereas

0885–3010/$25.00 © 2012 IEEE

the top was fixed in the x-direction. The contact between the simulated electrode and inclusion was modeled as bonded, whereas the contact between the electrode and background was assumed to be similar to lubricated metal plates [14], with a friction coefficient of 0.2. A sphere-of-influence mesh provided fine meshing near the inclusion and coarser meshing near the model boundaries. All phantom materials had a Poisson's ratio (ν) of 0.495; that is, nearly incompressible.

A transient structural analysis was used to simulate electrode vibration elastography. A Gaussian-shaped 100-μm-amplitude transient perturbation 10 ms in duration was applied in the y- (axial) direction to the top of the electrode, and shear wave propagation was simulated for an additional 20 ms, for a total duration of 30 ms. The simulation was discretized into 150 time steps for a frame rate of 5000 Hz, and y displacements were exported from ANSYS for shear wave velocity reconstruction assuming bidirectional wave propagation, as described in Section II-B.

The phantom and *ex vivo* experiments were similar to those previously reported in [13]. The phantom consisted of a stainless steel rod that was bonded to a stiff ellipsoidal inclusion simulating a radio-frequency ablation, which was in a softer background. The radio-frequency ablation was formed in fresh bovine tissue using a Cool-tip radio-frequency ablation system (Valleylab, Boulder, CO) and a radio-frequency electrode 1.5 mm in diameter (17-gauge) with a 2 cm active length. The electrode was inserted approximately 5 cm into the liver, and power was applied for 3 min using the radio-frequency generator's impedance-controlled power pulsing algorithm. Following imaging, the ablation was sliced along the imaging plane and photographed.

B. Shear Wave Velocity Reconstruction

Shear wave velocity reconstructions were compared assuming bidirectional or lateral wave propagation assumptions in finite element models, TM phantoms, and *ex vivo* bovine tissue. The time-to-peak algorithm was used to reconstruct shear wave velocity [7]; however, strictly lateral shear wave propagation was not assumed. In our approach, we estimated both lateral and axial gradients of the time-to-peak image, which were then compared on a pixel-by-pixel basis. The greater of the two gradients was the assumed wave propagation direction and was used as the velocity estimate for that particular pixel in a combined gradient image. Taking the inverse of this image yielded shear wave velocity, which was then compared with an image assuming strictly lateral wave propagation.

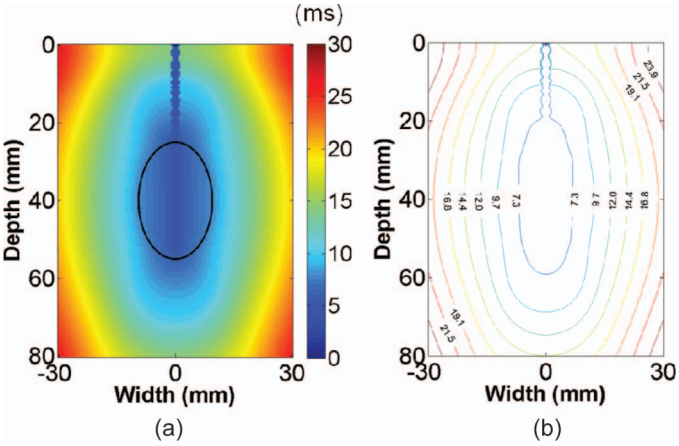

Fig. 1. Time-to-peak displacement from finite element simulation. The shear wave propagates more quickly in the hard inclusion than in the soft background. The contour map clearly shows axial and lateral wave propagation. Outline indicates inclusion periphery.

III. Results

Finite element modeling was used to investigate shear wave propagation. The shear wave propagates primarily laterally, but some axial wave propagation exists, as shown by the time-to-peak images in Fig. 1. In Fig. 2, the lateral gradient of the time-to-peak is much larger

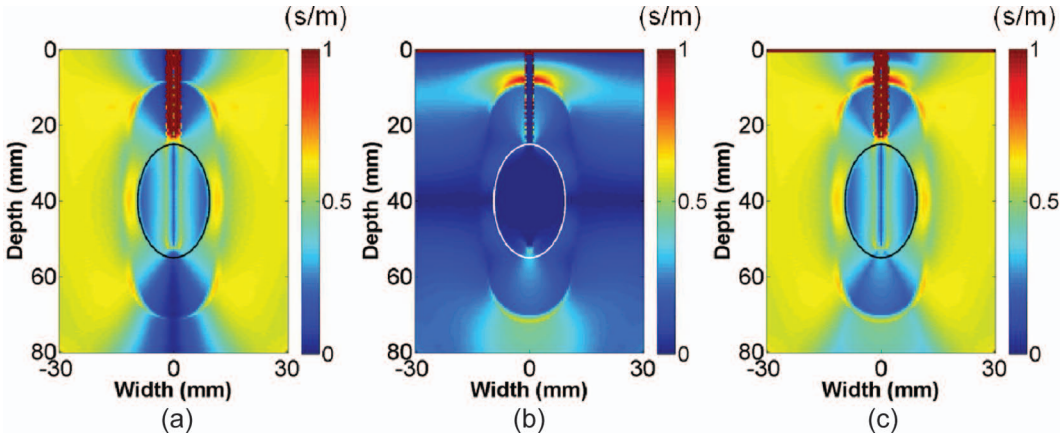

Fig. 2. Time-to-peak gradients from finite element simulation. The images in (a) and (b) show lateral and axial gradients, respectively. The combined gradient image in (c) shows the larger of the two gradients at each pixel location. The outline indicates the inclusion periphery.

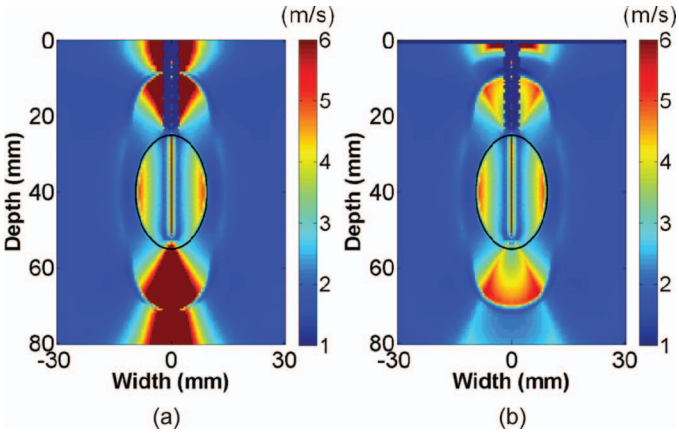

Fig. 3. Shear wave velocity images from finite element simulation. The shear wave velocity estimates in (a) assume only lateral wave propagation, whereas the estimates in (b) assume lateral and axial propagation. The artifacts in (a) are reduced in (b). The outline indicates the inclusion periphery.

than the axial gradient, except above and below the inclusion, as can be seen in the combined gradient image. The inverse of the time-to-peak gradients yields the shear wave velocity images shown in Fig. 3. Artifacts are present above and below the inclusion when assuming only lateral shear wave propagation, as in Fig. 3(a), but these are minimized when assuming bidirectional wave propagation, as in Fig. 3(b).

TABLE I. Ablation Area Estimates.

Experiment	Reference image	SWV lateral	SWV bi-directional
Phantom			
Area (mm^2)	418	474	433
Difference from B-mode (%)	—	13.4	3.6
Ex vivo			
Area (mm^2)	713	778	719
Difference from gross pathology (%)	—	9.1	0.8

SWV = shear wave velocity.

Experiments using a TM phantom provided similar results in Fig. 4. The lateral and axial gradients were used to create the combined gradient image. The shear wave velocity image assuming only lateral shear wave propagation provided well-defined inclusion borders on the ablation sides but some ambiguity on the top and bottom of the inclusion. Assuming bidirectional wave propagation minimizes these artifacts, providing a representation of the inclusion closer to that seen on the B-mode image. This is corroborated in Table I. Inclusion area on the shear wave velocity images was estimated by manually segmenting the inclusion from the background, assuming

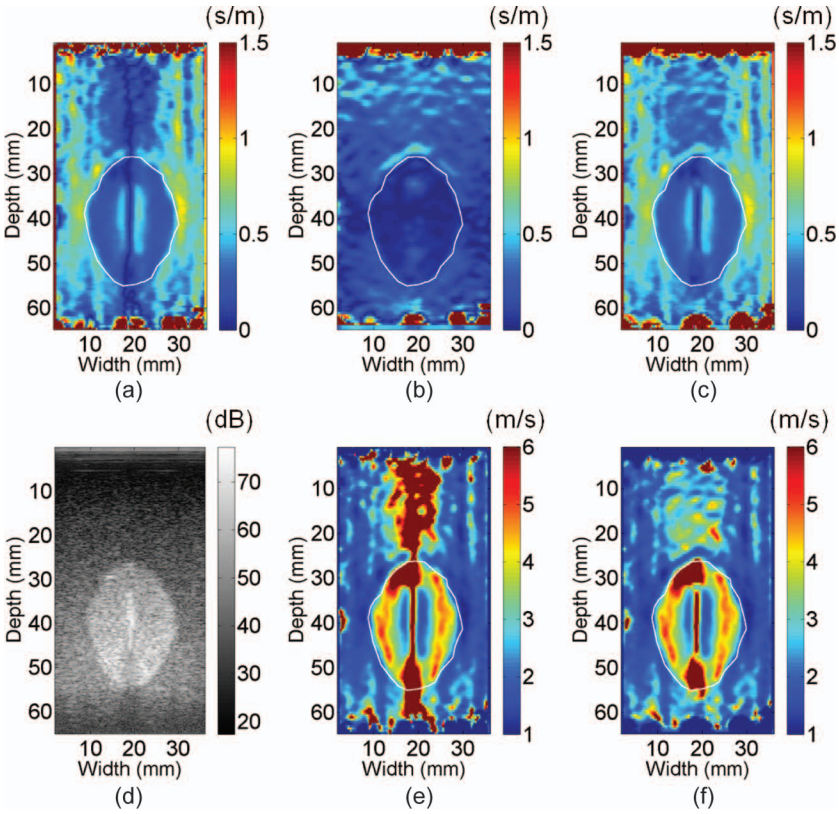

Fig. 4. A stiff-inclusion phantom simulating an ablated region. Images in (a), (b), and (c) show lateral, axial, and combined gradients, respectively. High time-to-peak gradients are present on the sides of the ablation in (a), on the top and bottom of the ablation in (b), and on all sides of the ablation in the combined image in (c). Echogenic contrast delineates the inclusion from the background in the B-mode image in (d). The shear wave velocity image in (e) assuming only lateral shear wave propagation has larger artifacts than (f), which assumes bidirectional propagation. White delineation in images signifies the B-mode inclusion periphery.

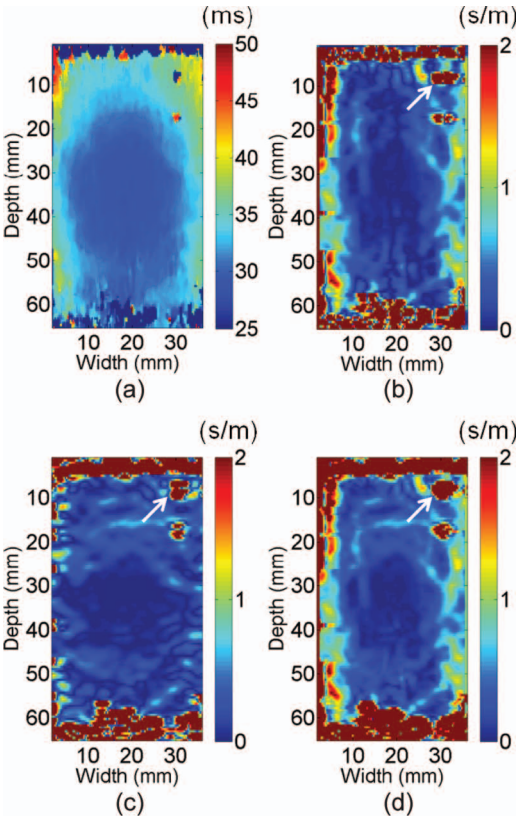

Fig. 5. Time-to-peak and gradients in an *ex vivo* radio-frequency ablation. Images show (a) time-to-peak, (b) lateral time-to-peak gradient, (c) axial time-to-peak gradient, and (d) combined time-to-peak gradient. The high gradient shown by the white arrows corresponds to a blood vessel shown in the gross pathology image in Fig. 6(b).

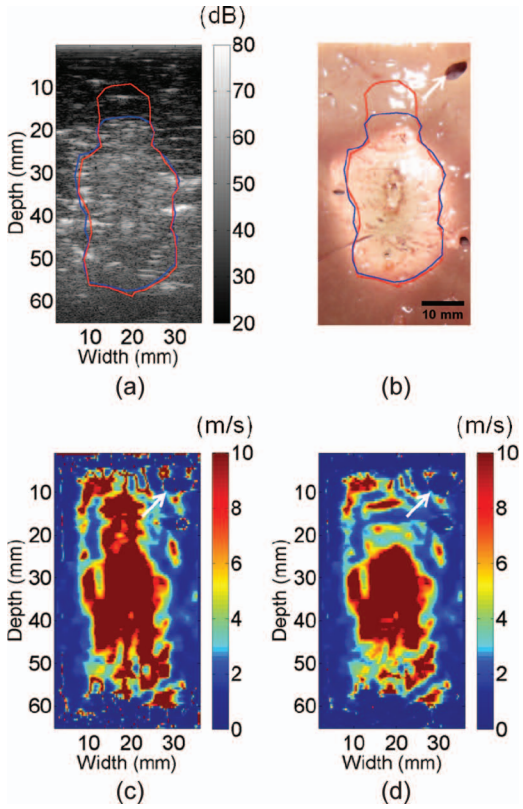

Fig. 6. *Ex vivo* ablation images. There is low echogenic contrast between the ablated and untreated tissue in the B-mode image in (a). Gross pathology in (b) shows the ablation and blood vessels in the imaging plane. One vessel, highlighted by the white arrow, appears as an artifact on the shear wave velocity images assuming (c) lateral or (d) bidirectional wave propagation. The artifacts in (d) are reduced compared with (c), and the ablation shape in (d) more closely resembles the gross pathology in (b).

the sharp velocity contrast corresponded to the inclusion periphery. The inclusion area on the shear wave velocity image was 13.4% greater than B-mode area when assuming lateral propagation, whereas the inclusion area assuming bidirectional propagation was only 3.6% greater.

Delineation improvements were also shown in an irregularly shaped radio-frequency ablation. In Fig. 5, large lateral gradients were present on the sides of the ablation, and large axial gradients were present on the top of the ablation. An artifact, indicated by the white arrow, was present in both the lateral and axial gradient images but was most defined in the combined gradient image. Shear wave velocity images are compared with B-mode and gross pathology in Fig. 6. In the B-mode image, ablation boundaries are vaguely discernable because of minimal echogenic contrast. The shear wave velocity image assuming lateral propagation contains an artifact above the ablation, which is minimized when assuming bidirectional propagation. The artifact in Fig. 5 corresponds to a region of low shear wave velocity in Fig. 6, as shown by the white arrow. The ablation boundaries were delineated on both wave velocity images, assuming the border corresponded to a sharp velocity contrast. The delineation of the velocity reconstruction assuming bidirectional propagation includes significantly less artifact above the ablation, and the area is closer to the area estimated from gross pathology, as shown in Table I. Both delineations lie slightly within the ablation borders as represented on the gross pathology image.

IV. Discussion

In this study, we sought to improve ablation representation on shear wave velocity images from electrode vibration elastography by minimizing artifacts above and below ablated regions. Finite element analysis showed wave propagation both laterally and axially. Accounting for this by assuming bidirectional wave propagation minimized artifacts above and below stiff inclusions in the simulated data, as well as in a phantom and *ex vivo* bovine liver ablation. The *ex vivo* ablation representation on the shear wave velocity image was much closer to that on the gross pathology image when assuming bidirectional versus only lateral wave propagation. More accurate ablation representation will likely improve physician confidence in complete tumor treatment and thus lower tumor recurrence rates.

The finite element model shows that artifacts in shear wave velocity images are minimized above and below the inclusion when assuming bidirectional wave propagation.

The artifacts are not entirely removed, which suggests a complex wave motion that is not purely shear. This seems plausible because the motion of the actuator and the interfaces and boundary conditions likely influence the wave propagation. There is also some propagation that is not entirely lateral or axial. However, wave propagation is approximately lateral and axial near the inclusion. From phantom and *ex vivo* delineations, we saw that area overestimation was reduced from 13.4% to 3.6% and 9.1% to 0.8%, respectively. The computation cost of calculating more directional gradients likely will not significantly improve boundary delineation near the inclusion. Lateral propagation dominated the combined image as expected, given the perturbation motion. The halo surrounding the inclusion likely occurs because the wave is propagating before the needle motion has ceased.

The TM phantom further demonstrated the benefits of assuming bidirectional wave propagation. The bidirectional assumption provides an image with an inclusion that is more clearly defined from the background. It also clarifies ambiguity that exists in a region of high shear wave velocity on the bottom of the inclusion when assuming purely lateral propagation. In this image, a high-modulus artifact extends beyond the bottom of the ablation, suggesting a very stiff region both inside and below the inclusion. However, when assuming bidirectional propagation, this region is confined within the ablation and appears to correspond to a region of low echogenicity in the B-mode image. This may result from the superglue applied to the rod to bond it to the inclusion, which may have both stiffened this region and lowered its echogenicity. Shear wave velocity reconstruction is not valid on the electrode, because it is the source of shear wave generation; however, the electrode is represented on the image as an artifact that may be useful as a landmark.

A radio-frequency ablation showed improvements in an irregularly-shaped stiff inclusion. The axial gradients contributed more to the combined image, likely resulting from the rather blunt ends of the ablation when compared with the ellipsoidal phantom inclusions. A high-gradient region was present in the upper right of the gradient images, indicated by the white arrow. This was best defined in the combined image and likely corresponds to the blood vessel highlighted in Fig. 6(b), showing the ability of the bidirectional assumption not only to improve ablation delineation but also highlight additional features within the transducer field of view. A vessel was not observed in the gross pathology image for the artifact below the one highlighted by the white arrow, but it is possible that the vessel lay just below the surface of the plane that was sliced.

Minimization of artifacts provided an ablation periphery much closer to that in the gross pathology image. The improvements occurred primarily above and below the ablation. The lateral delineations for both sets of assumptions were comparable, slightly within the ablation boundary on the gross pathology image. This is consistent with previous studies using strain or sonoelasticity imaging to delineate radio-frequency ablations, which have shown a consistent underestimation in ablation area [15]–[17]. This likely occurs because the periphery of the ablation approaches the stiffness of the untreated background, a result of active perfusion cooling outweighing heat conduction near the ablation edges [18], [19]. However, this underestimation may be a benefit clinically, because a conservative estimate of ablation extent is prudent to ensure complete treatment of the pathological target.

We have shown that assuming bidirectional wave propagation improves ablation representation on shear wave velocity images. We assumed that the vibration of the radio-frequency needle produced purely lateral and axial wave propagation. There likely are other propagation directions, but the gains in ablation delineation accuracy may be outweighed by computational cost. This approach may be more qualitative in nature because of the complex nature of the wave propagation resulting from actuator motion and ablation interfaces, but ablation boundary delineation is more crucial clinically than quantitative modulus estimates. The improvements also primarily affect regions directly above and below the inclusion. In the majority of the image, lateral propagation dominates. A more thorough investigation of artifacts resulting from inhomogeneities such as blood vessels present in both radio-frequency and microwave ablations is necessary and will be the focus of future work. The bidirectional approach provides a significant improvement to electrode vibration elastography that improves our confidence in thermal ablation delineation when using this technique.

Acknowledgments

The authors would like to thank Dr. C. Brace, Ph.D., and Ms. L. Sampson for advice and assistance with the *ex vivo* experiment.

References

[1] Y. C. Fung, *Biomechanics: Mechanical Properties of Living Tissues*. New York, NY: Springer, 1993.

[2] J. A. Carrión, F. Torres, G. Crespo, R. Miquel, J. C. Garcia-Valdecasas, M. Navasa, and X. Forns, "Liver stiffness identifies two different patterns of fibrosis progression in patients with hepatitis C virus recurrence after liver transplantation," *Hepatology*, vol. 51, pp. 23–34, Jan. 2010.

[3] J. Bercoff, M. Tanter, and M. Fink, "Supersonic shear imaging: A new technique for soft tissue elasticity mapping," *IEEE Trans. Ultrason. Ferroelectr. Freq. Control*, vol. 51, pp. 396–409, Apr. 2004.

[4] L. Sandrin, M. Tanter, J. L. Gennisson, S. Catheline, and M. Fink, "Shear elasticity probe for soft tissues with 1-D transient elastography," *IEEE Trans. Ultrason. Ferroelectr. Freq. Control*, vol. 49, pp. 436–446, Apr. 2002.

[5] L. Sandrin, M. Tanter, S. Catheline, and M. Fink, "Shear modulus imaging with 2-D transient elastography," *IEEE Trans. Ultrason. Ferroelectr. Freq. Control*, vol. 49, pp. 426–435, Apr. 2002.

[6] L. Sandrin, B. Fourquet, J. M. Hasquenoph, S. Yon, C. Fournier, F. Mal, C. Christidis, M. Ziol, B. Poulet, F. Kazemi, M. Beaugrand, and R. Palau, "Transient elastography: A new noninvasive method for assessment of hepatic fibrosis," *Ultrasound Med. Biol.*, vol. 29, pp. 1705–1713, Dec. 2003.

[7] M. L. Palmeri, M. H. Wang, J. J. Dahl, K. D. Frinkley, and K. R. Nightingale, "Quantifying hepatic shear modulus in vivo using

acoustic radiation force," *Ultrasound Med. Biol.*, vol. 34, pp. 546–558, Apr. 2008.

[8] A. P. Sarvazyan, O. V. Rudenko, S. D. Swanson, J. B. Fowlkes, and S. Y. Emelianov, "Shear wave elasticity imaging: A new ultrasonic technology of medical diagnostics," *Ultrasound Med. Biol.*, vol. 24, pp. 1419–1435, Nov. 1998.

[9] L. Huwart, F. Peeters, R. Sinkus, L. Annet, N. Salameh, L. C. ter Beek, Y. Horsmans, and B. E. Van Beers, "Liver fibrosis: Non-invasive assessment with MR elastography," *NMR Biomed.*, vol. 19, pp. 173–179, Apr. 2006.

[10] S. A. McAleavey, M. Menon, and J. Orszulak, "Shear-modulus estimation by application of spatially-modulated impulsive acoustic radiation force," *Ultrason. Imaging*, vol. 29, pp. 87–104, Apr. 2007.

[11] M. Orescanin and M. Insana, "Shear modulus estimation with vibrating needle stimulation," *IEEE Trans. Ultrason. Ferroelectr. Freq. Control*, vol. 57, pp. 1358–1367, Jun. 2010.

[12] Q. C. Chan, G. Li, R. L. Ehman, P. J. Rossman, G. Cao, R. Li, and E. S. Yang, "Shear waves induced by moving needle in MR elastography," *Conf. Proc. IEEE Eng. Med. Biol. Soc.*, vol. 2, pp. 1022–1024, 2004.

[13] R. J. DeWall, T. Varghese, and E. L. Madsen, "Shear wave velocity imaging using transient electrode perturbation: Phantom and ex vivo validation," *IEEE Trans. Med. Imaging*, vol. 30, pp. 666–678, Mar. 2011.

[14] R. A. Serway and J. W. Jewett, Jr., *Physics for Scientists and Engineers*. Belmont, CA: Thomson-Brooks/Cole, 2004.

[15] T. Varghese, U. Techavipoo, W. Liu, J. A. Zagzebski, Q. Chen, G. Frank, and F. T. Lee Jr., "Elastographic measurement of the area and volume of thermal lesions resulting from radiofrequency ablation: Pathologic correlation," *AJR Am. J. Roentgenol.*, vol. 181, pp. 701–707, Sep. 2003.

[16] U. Techavipoo, T. Varghese, J. A. Zagzebski, Q. Chen, and W. Liu, "Semiautomated thermal lesion segmentation for three-dimensional elastographic imaging," *Ultrasound Med. Biol.*, vol. 30, pp. 655–664, May 2004.

[17] M. Zhang, B. Castaneda, J. Christensen, W. Saad, K. Bylund, K. Hoyt, J. G. Strang, D. J. Rubens, and K. J. Parker, "Real-time sonoelastography of hepatic thermal lesions in a swine model," *Med. Phys.*, vol. 35, pp. 4132–4141, Sep. 2008.

[18] K. S. Lehmann, J. P. Ritz, S. Valdeig, V. Knappe, A. Schenk, A. Weihusen, C. Rieder, C. Holmer, U. Zurbuchen, P. Hoffmann, H. O. Peitgen, H. J. Buhr, and B. B. Frericks, "Ex situ quantification of the cooling effect of liver vessels on radiofrequency ablation," *Langenbecks Arch. Surg.*, vol. 394, pp. 475–481, May 2009.

[19] B. B. Frericks, J. P. Ritz, T. Albrecht, S. Valdeig, A. Schenk, K. J. Wolf, and K. Lehmann, "Influence of intrahepatic vessels on volume and shape of percutaneous thermal ablation zones: In vivo evaluation in a porcine model," *Invest. Radiol.*, vol. 43, pp. 211–218, Apr. 2008.